Mine Water and the Environment (2019) 38:632–642
https://doi.org/10.1007/s10230-019-00609-1

TECHNICAL ARTICLE

Investigations into Mining-Induced Stress–Fracture–Seepage Field Coupling in a Complex Hydrogeology Environment: A Case Study in the Bulianta Colliery

Tong Zhang[1,4] · Yixin Zhao[2,4] · Quan Gan[3] · Xiaodong Nie[6] · Guangpei Zhu[5] · Yong Hu[4]

Received: 2 May 2018 / Accepted: 15 May 2019 / Published online: 30 May 2019

Abstract

The effect of mining-induced multi-physics coupling, characterized by stress–fracture–seepage field coupling (SFCC), is critical to safe mining and environmental protection. We investigated the spatiotemporal characteristics of the SFCC at the #31401 panel of the Bulianta Colliery. Changes in overburden movement, groundwater level, and groundwater inrush were monitored by means of borehole and working face observations, water leakage, and real-time video imaging. The results indicate that the distribution of mining-induced fractures was dominated by the key stratum, distributed as a "ladder shape" 30–75 m above the coal seam. The fracture penetrated into the lower key stratum and developed into the confined aquifer with a height of 140.5–154.0 m, while being truncated by the higher key stratum. Horizontal and vertical fractures developed sequentially in the confined aquifer-disturbed zone. Initiation, propagation, and interconnection of the seepage channel occurred in the fracture field, mediated by the redistributed stress. An abnormal discharge of 120–300 m^3/h along the direction of mining commenced at the transition of the lower key stratum to the higher key stratum, and concentrated below the Bulian Gully. A fracture height model was developed based on the vertical fracture propagation, and mining parameters were modified, including reducing the mining height and increasing the advance rate and support resistance of the longwall mining face to effectively reduce the SFCC effect.

Keywords SFCC · Key stratum · Confined aquifer · Seepage channel · Fracture height model · China

Introduction

Interest has been increasing in multi-field coupling behavior in the areas of nuclear waste disposal, hydrocarbon resource extraction, groundwater contamination, and municipal engineering, along with greater demands for coordinating the development of natural resources with sound engineering safety requirements and environmental protection. This is especially the case for underground mining, which can have a significant impact on the surrounding environment. Numerous research efforts on ground control, water inrush prevention, and stress redistribution have been conducted to explore the characteristics and interpret the mechanisms of mining-induced behavior in the surrounding rock. Simultaneously, substantial creative concepts, including aquifer protection mining (Zhang et al. 2011), precise mining (Yuan 2017; Yuan et al. 2017a, b), and underground reservoir (Gu 2015) and mined space development (Xie et al. 2017) have been proposed. These concepts all attempt to achieve the goal of precisely coordinated resource mining in multiple

✉ Tong Zhang
1099731996@qq.com

1 State Key Laboratory of Mining Response and Disaster Prevention and Control in Deep Coal Mines, Anhui University of Science & Technology, Huainan 232001, Anhui, China

2 School of Energy & Mining Engineering, China University of Mining & Technology (Beijing), Beijing 100083, China

3 Department of Petroleum Geology and Geology, School of Geosciences, University of Aberdeen, Aberdeen, UK

4 Beijing Key Laboratory for Precise Mining of Intergrown Energy and Resources, China, University of Mining & Technology (Beijing), Beijing 100083, China

5 College of Engineering, Peking University, Beijing 100871, China

6 School of Mechanics and Civil Engineering, China University of Mining and Technology (Beijing), Beijing 100083, China

energy stacks (e.g. coal, gas, oil and other fossil and natural resources) in areas such as the Ordos Basin, by considering the effect of stress–fracture–seepage field coupling (SFCC).

The behavior of vertical mining-induced fractures in underground mines has been widely studied, and four zones have been identified above the panel goaf: successively, the caved, fractured, continuous deformation, and soil zones (Booth and Spande 1992; Chekan and Listak 1993; Palchik 1989; Singh and Kendorski 1981). Among these, the caved and fractured zones have drawn more attention, as they are directly related to mine safety and the protection of associated resources. Parallel to the panel goaf, the fracture field is characterised by dome, horse saddle, or flat profiles. Field monitoring and physical and numerical simulation (Xie et al. 2009; Zhao et al. 2015) is used to predict the maximum height of the destressed zone (Majdi et al. 2012a, b; Rezaei et al. 2015).

In addition, the maximum height of the fracture field is significantly dependent on mining hydrogeology. Denkhaus (1964) pointed out that for a dome with sufficient cohesion, the maximum height of the fracture is up to 50% of the depth of the cover, compared to 63% in insufficiently cohesive material. Other similar investigations are shown in Table 1 (Guo et al. 2012; Lu et al. 2011; Palchik 2003; Kelly et al. 2002; Shabanimashcool and Li 2012; Xie et al. 2009; Zhang et al. 2011). Geometric dimension also plays an important role; Fawcett et al. (1986) predicted a greater fracture height at typical panel widths between 100 and 200 m. Five theoretical models have been developed based on coal seam thickness and expansion factors (Majdi et al. 2012a, b), which conclude that for short and long term conditions, the maximum height of the fracture field corresponds to 6.5–24 and 11.5–46.5 times the extracted coal seam thickness, respectively.

An increasing amount of research has been motivated by the desire to control or predict the mining-induced behavior of the surrounding rock, accompanied by the effects on aquifers. Booth and Spande (1992) suggested that different forms of deformation at various levels within the overburden will induce hydraulic changes as a response to mining. According to Karacan et al. (2007), permeability can vary widely in different locations and for different roof rocks in the caved zone because permeability depends on the type of rock units, the extent of their fragmentation and packing in the mined void, and the caving height. Singh and Kendorski (1981) and Karacan and Goodman (2009) evaluated the disturbance of rock strata resulting from mining beneath surface water and waste impoundments; their work identified an aquiclude zone with unmodified permeability located at a height about 30 times the seam thickness above the seam. Xu et al. (2010) developed the model of the fractured zone for different mining conditions, applying it to 40% of the mining area beneath the Xiaolangdi reservoir.

For the dynamic interaction between the fracture and stress fields, the key strata theory (Qian 2003) provides an excellent interpretation of the governing rules of overburden crack propagation and distribution caused by redistributed stress. Subsequently, the stress shell hypothesis (Xie et al. 2009), which is similar to the pressure arch hypothesis (Kratzsch 1983), gives an insight into the distribution and formation of the stress–fracture–seepage field with the associated macro-stress shell. According to this theory, the shell bears and transfers the loads of the overlying strata, and acts as the primary supporting system of forces for the underlying fractured zone. However, basic experiments (Tan et al. 2014; Yuan et al. 2016, 2017a, b; Zheng et al. 2015) and engineering practices (Yang et al. 2007; Zhang et al. 2011) demonstrate that seepage flow significantly contributes to the development of the fracture-stress field; meanwhile, the growth and propagation of stress-dependent fractures dynamically mediates seepage behavior. Consequently, investigating the evolution of mining-induced SFCC and

Table 1 Maximum height of fracture for different hydrogeology conditions

Mining site	Maximum height of fracture (m)	Mining height (m)	Hydrogeology	Method	Reference
American	72.7–85.3	2.44	Limestone, sandstone, clay shale	In-situ	Guo et al. (2012)
Longdong coal mine, China	36–37	4	Unconsolidated alluvium, aquifer, mudstone, sandstone	Numerical/physical	Lu et al. (2011)
Torezko-snezhnyanskaya area, Ukaine	88.57–140.07	0.9–1.6	Limestone, sandstone, calcareous shale	In-situ	Palchik (2003)
Appin Colliery, Sydney Basin	50–70	2.3	Sandstone	In-situ	Kelly et al. (2002)
Svea nord, Arctic area	110	4	Sandstone, siltstone, glacier surface	In-situ/numerical	Shabanimashcool and Li (2012)
Xieqiao, China	130	5.4	Mudstone, siltstone, packsand	Physical/numerical	Xie et al. (2009)
Shangwan colliery, China	58–63.8	5.8	mudstone, sandstone, Alluvial sand, Xiasha gully	In-situ	Zhang et al. (2011)

discovering their associated characteristics will contribute to coordinated mining, accommodating aquifer protection, protection of weakened surface ecology, prevention of water inrush catastrophes, and the reuse of abandoned mining space.

This research focused on multi-field coupling evolution and associated characteristics in a mining excavation in a complex hydrogeological environment in the #31401 panel of the Bulianta Colliery. Field monitoring data of overburden movement, aquifer level changes, and face-inrush variations were analyzed. Finally, the SFCC mechanism was analyzed, a model of fracture height based on the vertical fracture propagation criteria was proposed, and the mining parameters were modified to effectively reduce the effect of the SFCC.

Hydrogeology

The #31401 panel of the no. 1–2 coal seam was 4.63 km long and 265.25 m wide. The seam dip angle ranged from 1 to 3° and the thickness was 3.0 to 6.08 m, with an average design excavation height of 5.2 m. The thickness of the overlying bedrock decreased gradually from 190 to 120 m as mining progressed. The 30–80 m thick confined aquifer is mainly constituted of conglomerate and coarse sandstone from the sedimentary layer of the Lower Cretaceous and Upper Jurassic. The unconsolidated aquifer was 5–30 m thick and consisted mostly of sandstone. Notably, there was a powerful hydraulic connection between the unconsolidated and confined aquifers that formed a composite aquifer that was 38–110 m thick. However,

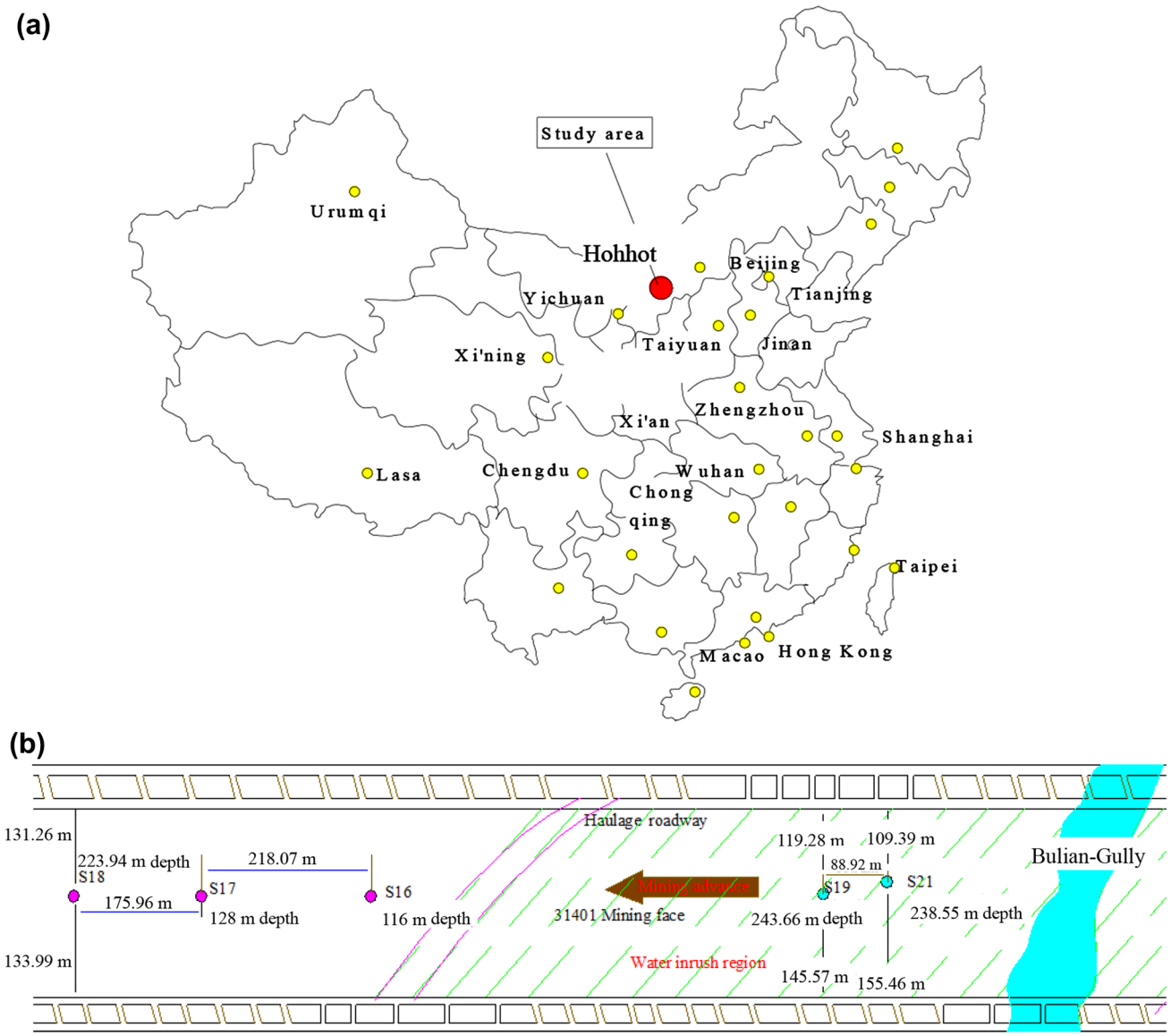

Fig. 1 **a** Colliery location, **b** layout of the #31401 panel

the confined aquifer was characterised by abundant water and lower permeability before mining. The discharge was 0.00147 L s^{-1} m^{-1}, as observed by boreholes. A surface gully named Bulian Gully is located above the middle of the #31401 panel, with a discharge of 60–80 m^3/h. The colliery site and specific layout of the mining panel are shown in Fig. 1a, b, respectively. The stratigraphic columns of the panel, represented by B269, Bk27, and B261, are shown in Fig. 2.

The Setup of the Field Measurement

A series of boreholes were drilled vertically from the surface to the bottom of the stratum overlying the coal seam as mining advanced in order to observe the movement of the overburden strata, propagation of mining-induced cracks, and water inrush behavior. Integrated monitoring technology, including borehole observation and real-time video imaging, was employed. The complicated hydrogeological region around the Bulian Gully was identified as a key research zone (Fig. 1b). The following elements were monitored:

(a) To monitor the movement of overburden strata along the center of the dip direction, monitoring borehole S18 was drilled at a distance of 133.99 m from the tailgate and 131.26 m from the headgate, while a multi-point roof extensometer was installed. The extensometer has three anchors located at the surface, confined aquifer, and bedrock, corresponding to depths of 0, 130, and 180 m, respectively, relative to the ground surface. Boreholes S17 and S16 ahead of longwall mining face (LMF) were positioned at the centerline of the mining panel at distances of 175.96 and 394.03 m from S18; the corresponding depths were 128 and 116 m, respectively.

(b) To monitor crack development around the maximum discharge area (2.16 km in front of the open-off cut), boreholes S19 and S21 were drilled post-mining around the panel center at depths of 119.28 and 238.55 m and at distances of 16.95 and 105.87 m from the maximum discharge position. Integrated monitoring technology was applied in S19 and S21 to record the dynamic fracturing behavior and the response of the seepage fluids.

(c) The behavior of fluid flow and surrounding rock was synchronously recorded as the LMF advanced.

Double column shield hydraulic support, including 4.3/5.5 m supports produced by Joy and 5.5 m supports made in China, was used for working face support. The coal cutter had a mining height of 2.7–5.4 m. The mining speed was controlled within 10 m/d.

Results and Analysis

Key Stratum Distribution

Based on the stratigraphic lithology of boreholes B274, B269, Bk27, Bks4, B261, and B257, and using the software of KSPB (Xu and Qian 2000), the key stratum in the bedrock were recognized (Fig. 3). Figure 3 shows that the distribution of the key stratum in #31401 panel has

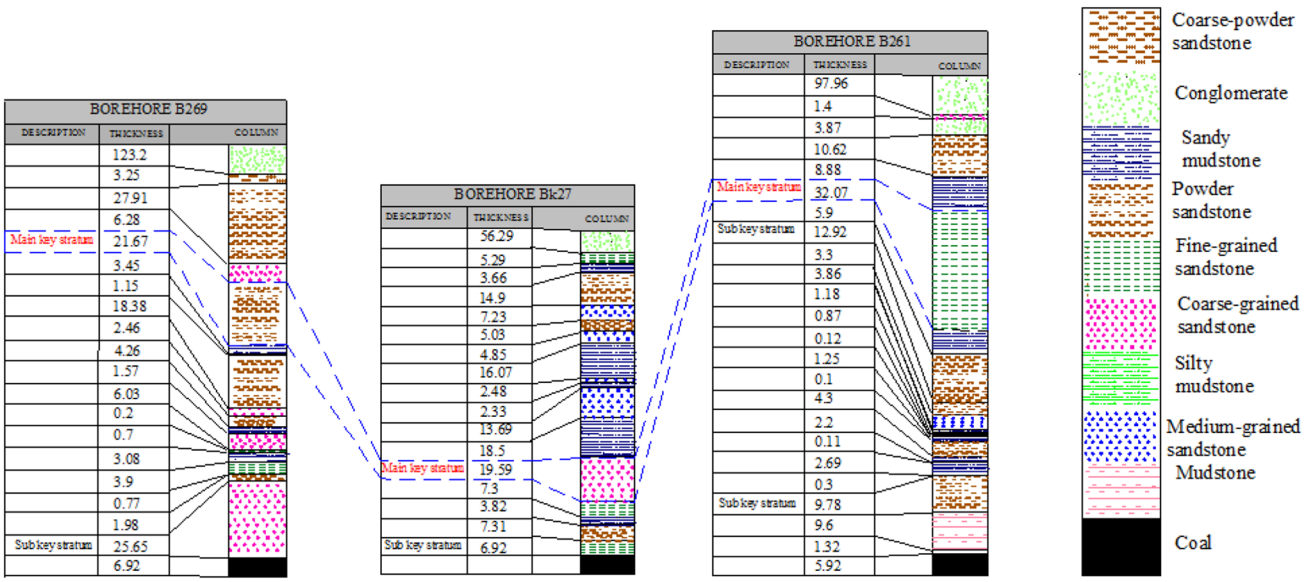

Fig. 2 Stratigraphic columns for the #31401 panel

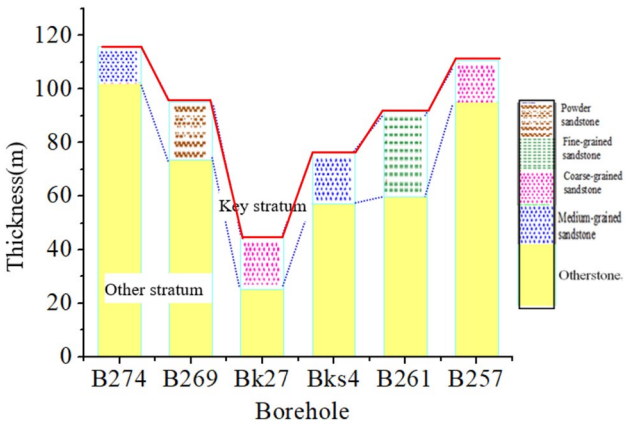

Fig. 3 Measured key strata distribution for the #31401 panel

a "ladder shape," with an associated depth difference of 30–75 m. In detail, the distance between the coal seam and key stratum ranged from 30 to 60 m for the middle zone; however, at the two end edges, it ranges from 70 to 105 m.

Overburden Strata Movement

A multi-point roof extensometer was installed in borehole S18 to verify that the movement of the overburden strata is governed by the key stratum. The position of each anchor and its corresponding monitoring results are shown in Fig. 4, which illustrates the slight movement of the key stratum was presented as the LMF advanced 19.65 m beyond S18. This indicates that the growth of the fracture was triggered and the propagation scope of the fracture became larger and larger as mining advanced.

Subsequently, the displacement velocity showed a sharp increase when the LMF advanced 36.6 m beyond S18 at a constant acceleration rate of the displacement until it reached 100 m. During this period, a larger increment in displacement occurred in the key stratum. Then, from 100 to 200 m, the displacement velocity decreased progressively, and stabilized after 200 m. By contrast, the displacement in the bedrock and confined aquifer occurred at 50 m, later than that of the key stratum; thereafter, it maintained a similar development pattern compared with the movement of the key stratum. This demonstrates that the key stratum was located in the bedrock and played a vital control role in fracture propagation and overburden strata movement during mining. With the protection of an intact key stratum, the overburden strata remained stable without the disturbance of fractures; however, as cracks penetrated the key stratum and propagated into the overlying strata, the key stratum presented less strength and started to synchronously sink with the overlaying strata.

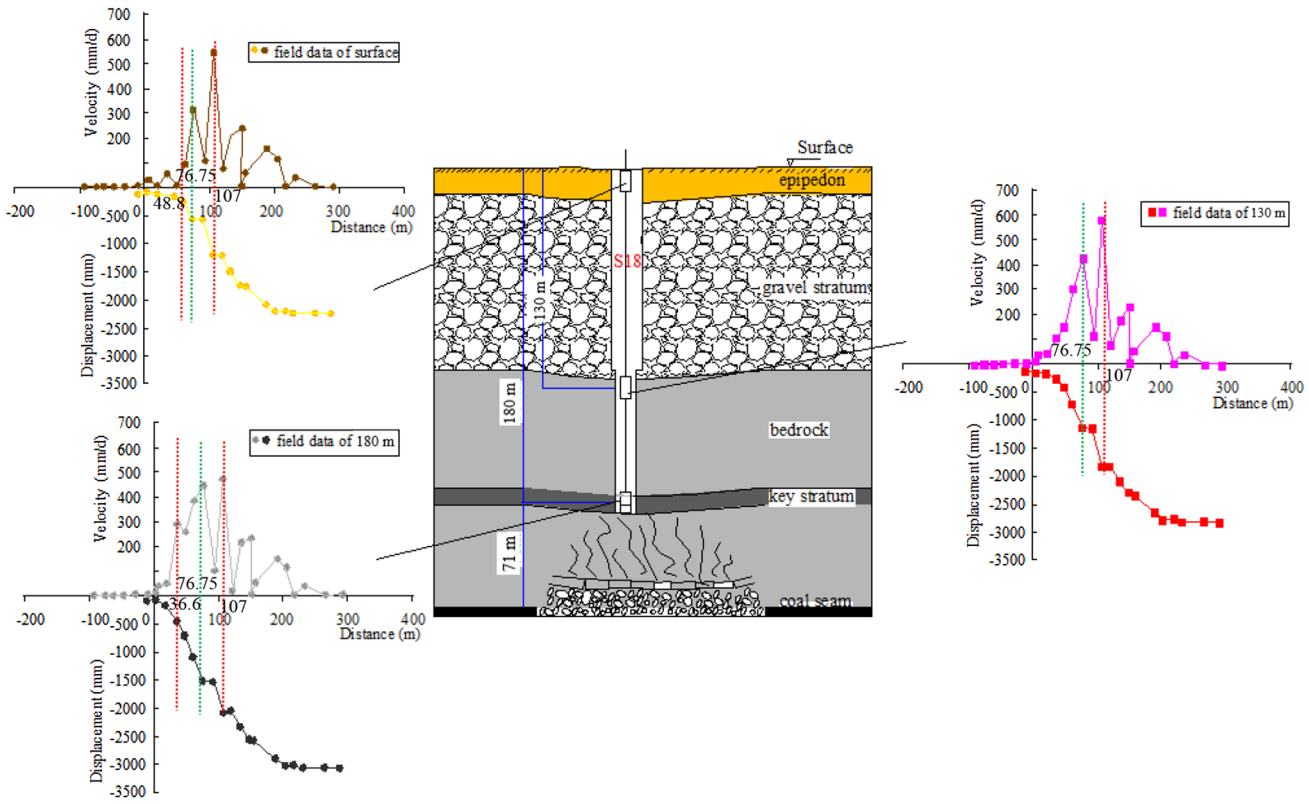

Fig. 4 Measured overburden strata movement

Mining-Induced Fracture Evolution

Water level variations were obtained by borehole observations at S17, S16, S19, and S21. Figure 5 shows that a violent variation occurred in the confined aquifer as mining approached within 30 m of S17. Subsequently, as the LMF advanced from 20 to 55 m away from S17, the water level dropped dramatically. At 55 m, the water was gone, indicating that the fracture had propagated into the base area of the confined aquifer. After that, the water level tended to recover, increasing sharply approaching 112 m behind the LMF, indicating that the redistributed stress promoted water recovery by preventing fracture initiation, propagation, and coalescence and thereby reducing the hydraulic conductivity in the fractured rock mass. Fracturing was limited below the confined aquifer near S16, as demonstrated by the negligible fluctuation of the water level. In contrast, the confined aquifer was influenced by stress-dependent fractures at S19 and S21, as characterized by the dramatic disappearance of water at a depth of 90 m; the corresponding maximum fracture heights reached 154.0 and 140.5 m above the mining panel, respectively. As the boreholes were continuously drilled to depths of 223.52 and 217.88 m, the caving zone was discovered, as characterized by drilling resistance at maximum heights of 17.08 and 19.72 m for S19 and S21, respectively.

The response to the fracture-seepage field coupling was identified by real-time video imaging of borehole S21 (Fig. 6). Specifically, at depths of 38–73 m, the discharge velocity increased gradually; horizontal fracturing was observed at a depth of 73 m. At a depth of 79 m, fracturing was observed as high porosity, due to movement of the conglomerate aquifer. At a depth of 94 m, many horizontal fractures appeared. At depths of 102 and 130 m, the discharge velocity drastically increased with depth, which can be attributed to the increased fluid pressure and growth of the horizontal fractures. Vertical fracturing intensively initiated, propagated, and coalesced with the horizontal fracture during the following months, and was observed as fracturing at the ground surface (Fig. 7). It is evident that geological conditions significantly affect the development of overburden strata movement and fracture propagation, as represented by the negative correlation between the height of the mining-induced fracture and the key stratum location, such that S17 and S16, located in the higher key stratum, had a lower fracture height, and S19 and S21, located in the lower key stratum, had a greater fracture height.

LMF Discharge

Figure 8 shows that compared to the average discharge value of 50–80 m^3/h, several incidences of abnormal water inrush occurred along the strike direction. The maximum discharge occurred 2164 m ahead of the open-off cut; at 2420, 2485, and 2552 m in the lower stratum zone, relatively less abnormal discharges, ranging from 120 to 200 m^3/h, occurred, compared to others that varied from 200 to 300 m^3/h in the higher stratum zone. In addition, an abnormal discharge of

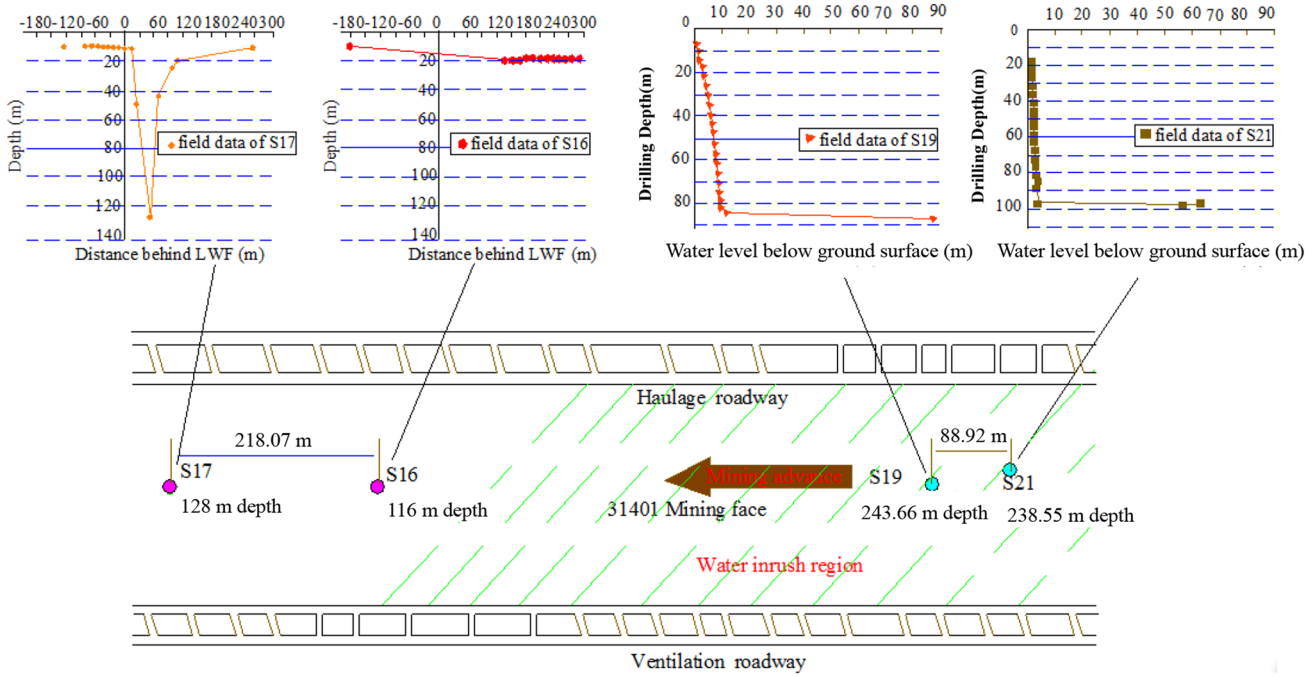

Fig. 5 Measured fracture distribution in the #31401 panel

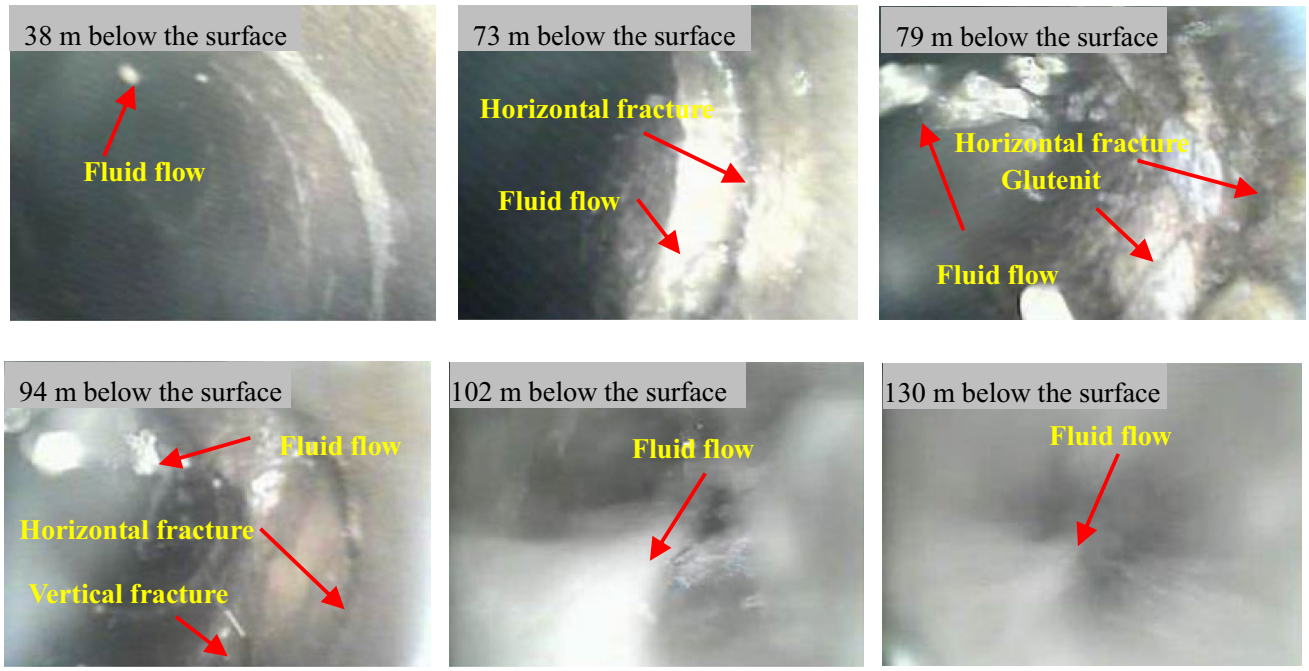

Fig. 6 Real-time video imaging of the S21 in different deep

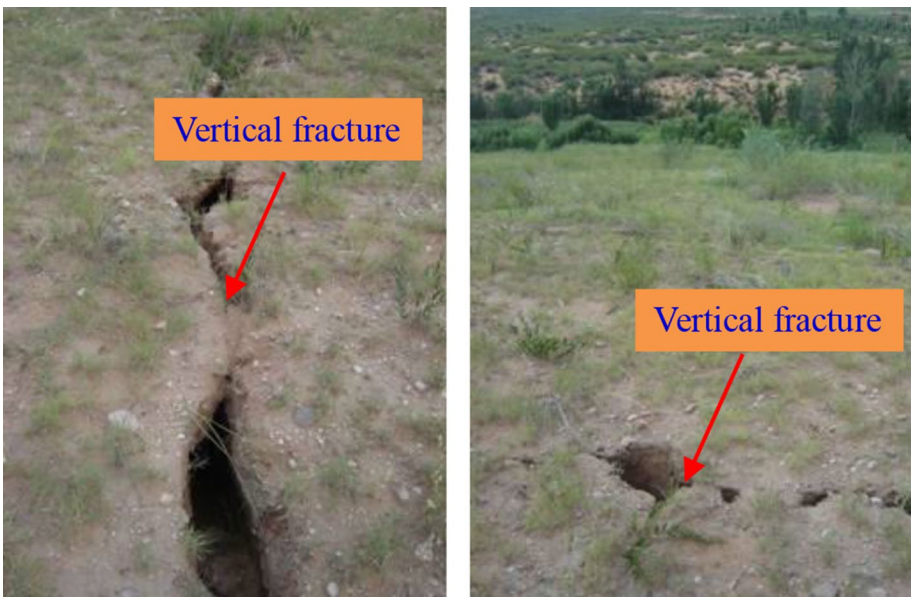

Fig. 7 Vertical fracture around borehole S19 and S21

120–300 m^3/h along the mining direction commenced in the transition zone between the higher and lower zones. Notably, the three points (i.e. at 2420, 2485, and 2552 m) were all close to the dividing boundary between the water inrush and safe regions, while the relatively larger abnormal discharge positions were concentrated below the Bulian Gully. It can be seen that the geology and hydrology represented by the key stratum and Bulian Gully both contributed to the abnormal water inrush behavior of the LMF. The key stratum controls the growth, propagation, and closure of fractures caused by the concentrated stress due to mining; the seepage source contributes to the opening of these fractures and the growth of new cracks by reducing the effective stress and by increasing the fluid pressure.

The LMF Responds to Redistributed Stress

Based on field measurements, given its complicated roof structure, the LMF usually had high supporting pressure accompanied by significant rib spalling, roof leakage, step

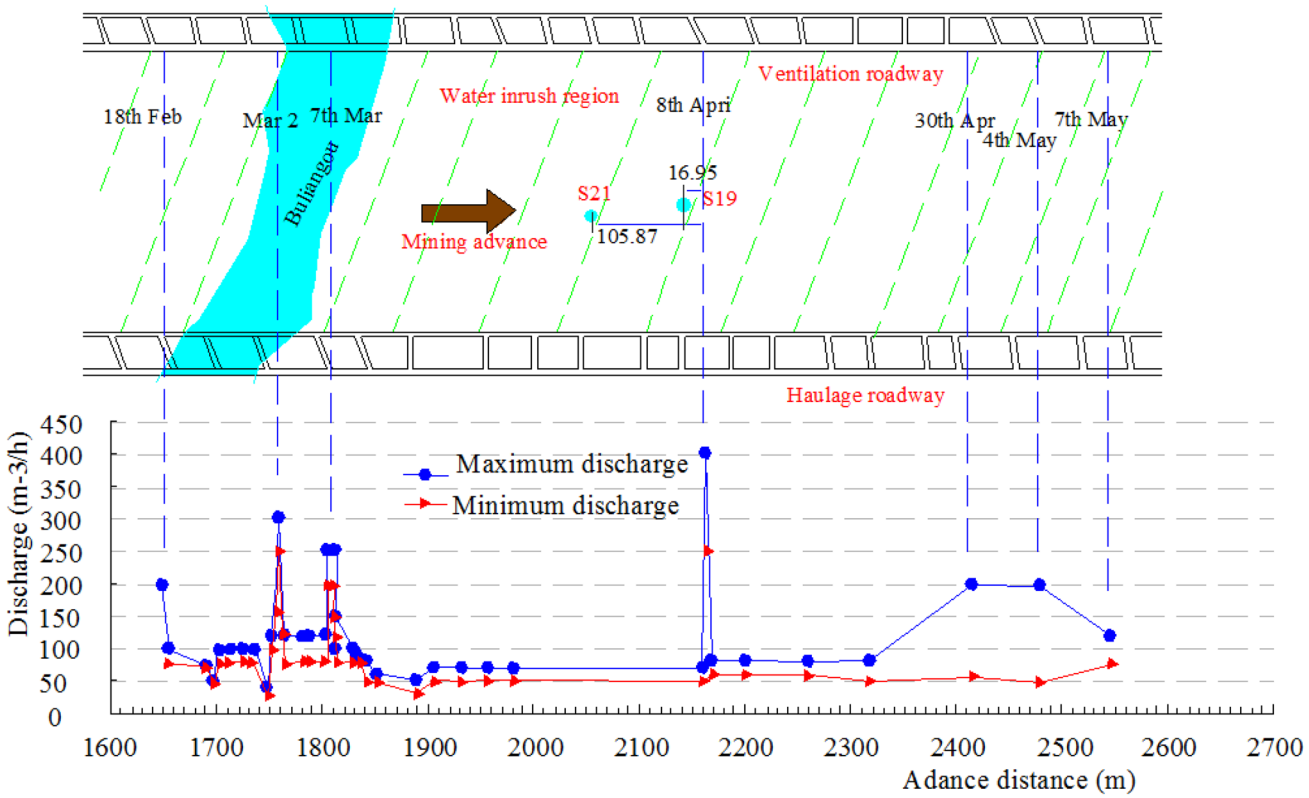

Fig. 8 Measured discharge condition of the LMF

subsidence, and support inclination in response to redistributed stress. For the high probability areas of water inrush, such as S19 and S20, the LMF supporting pressure increased irregularly, and was accompanied by multi-point leakage and 3–4 m of roof caving. Simultaneously, the discharge of the stope was significantly correlated with periodic weighting; i.e. larger increments of discharge corresponded to high periodic weighting.

The Accommodation Strategy

The SFCC Mechanism

The results of field monitoring indicate that the behavior of multi-field coupling was significantly influenced by the mining geology and hydrology, which is represented by the abnormal discharge near the overlying gully and the difference in the maximum fracture height between the lower and higher key strata. The corresponding mechanisms are presented as follows:

1. Due to the separation between the lower separated layer (considering a totally compressed situation) and the key stratum, the separation space for the lower key stratum was greater than or equal to the maximum deflection of the key stratum. The fracture penetrated the key stratum and propagated into the overlying strata, resulting in the rupture of the key stratum and the occurrence of seepage. Simultaneously, the discharge of the LMF displayed periodic variations that were associated with the periodic rupturing of the main roof. For the higher key stratum, the separation space was less than the maximum deflection of the key stratum, the key stratum remained intact, the maximum height of the fracture field was under the key stratum, and seepage was prevented in the fractured zone.
2. Under the integrated influence of the lower key stratum and activated confined aquifer, a transition zone corresponding to the diving boundary of the water inrush region was characterized by high conductivity channels. These channels were induced by a coupled hydro-mechanical effect (i.e. the interaction between the high fluid pressure and the lower redistributed stress). This eventually contributed to an abnormal water inrush at the working face.
3. As the LMF advances, the main roof will periodically rupture, which will contribute to more fracturing and promote water inrush events. As more violent overburden loads are released at the unstable area of the overlying strata, more concentrated fractures will be created

near the LMF, and the maximum LMF discharge will occur.

The Fracture Height Model

According to Qian (2003), the separation space and the maximum deflection of the overlying stratum can be derived according to Eqs. 5–8:

$$\Delta H = \sum_{i=1}^{m} h_i + M - K_i \sum_{i=1}^{m} h_i \tag{5}$$

$$E_{i+1} I_{i+1} W_{i+1} = -\frac{q_{i+1}}{12} L_{i+1} x^3 + \frac{q_{i+1}}{24} x^4 + \frac{q_{i+1}}{24} L_{i+1}^2 x^2 + C_1 x + C_2 \tag{6}$$

$$I_{i+1} = \frac{b}{12} h_{i+1}^3 \tag{7}$$

$$L_{i+1} = h_{i+1} \sqrt{\frac{2R_{t(i+1)}}{q_{i+1}}} \tag{8}$$

Considering the initial condition of $x=0$, $w=0$; $x=\mathrm{L}$, $w=0$; $b=1$, corresponding to the maximum deflection location of $x=L/5$, and substituting Eqs. 7 and 8 into Eq. 6, the maximum deflection of the key stratum is expressed as:

$$W_{\max(i+1)} = \frac{32}{625} \frac{h_{i+1} R_{t(i+1)}^2}{E_{i+1} q_{i+1}} \tag{9}$$

Combining Eq. 5 and 9, the criteria for the propagation of the vertical fracture was obtained:

$$M - \frac{32}{625} \frac{h_{i+1} R_{t(i+1)}^2}{E_{i+1} q_{i+1}} \geq \sum_{i=1}^{m} K_i h_i - \sum_{i=1}^{m} h_i \tag{10}$$

Finally, the final height of the fracture field can be confirmed as the vertical fractures are truncated by the overlying stratum with high strength:

$$M - \frac{32}{625} \frac{h_{i+1} R_{t(i+1)}^2}{E_{i+1} q_{i+1}} \leq \sum_{i=1}^{m} K_i h_i - \sum_{i=1}^{m} h_i \tag{11}$$

$$H = \sum_{i=1}^{m} h_i + M \tag{12}$$

where m is equal to 1, 2, 3….n, H is the height of the fracture field, ΔH is the space height between adjacent strata I and $i+1$, M is the mining height, K_i is the expansion coefficient of each overburden stratum, which is a function of time, h_i is the thickness of each overburden stratum i, q_{i+1} is the unit loading for overlying stratum i + 1, L_{i+1}, E_{i+1}, $R_{t(i+1)}$, $W_{max(i+1)}$ is the limit span, elastic modulus, tensile strength, and maximum deflection of the overlying stratum $i+1$.

Through Eqs. (10), (11), and (12), it can be observed that the fracture height is a function of the location thickness, strength, and unit loading of the overlaying strata. The difference in the mechanical properties of dry and saturated sandstone was determined by Chen et al. (2014) and Xiong et al. (2011), who determined that rock strength is weakened by the effect of the fluid. As a result, fracture height is increased by the influence of the confined aquifer. The higher the key stratum location, the less the key stratum unit loading, and vice versa, with a constant value of thickness and strength of the key stratum. So it is clear that in this study, the probability that a fracture would penetrate the key stratum was greater for the lower key stratum than for the higher key stratum, and the height of the fracture was greater beneath Bulian Gully (Fig. 9). The transition zone between the higher and lower key strata was the trigger of the water inrush, which occurred when the fracture height peaked.

Implementation

Preventing the development of fractures that penetrate the key stratum in different hydrogeological conditions and blocking the high conductivity channels that are formed is the key way to reduce the effect of multi-field coupling efficiently. However, the rupture of the key stratum is governed by the separation space and dynamic strength of the key stratum. Therefore, reducing the excavation height, grouting localized backfill, and increasing the advance rate (which corresponds with large fracture heights) are better choices for engineering practice, especially in sensitive areas such as the under the surface water gully and in the transition zone. In this study, the effect of multi-field coupling was reduced successfully by decreasing the mining height to 2.78–3 m, accelerating the advance rate to 13~16 m/d, and enhancing the LMF support resistance to 10,800–11,900 kN in locations of complex hydrogeology in panel #31401.

Conclusions

Based on the field monitoring results, we concluded that the location of the key stratum and seepage source significantly affect the degree of SFCC. For the lower key stratum, fracturing penetrated the key stratum and propagated into the confined aquifer, triggering the seepage field of the stope. The presence of the replenishment source resulted in frequent abnormal water inrush events below the overlying gully. Key conclusions were:

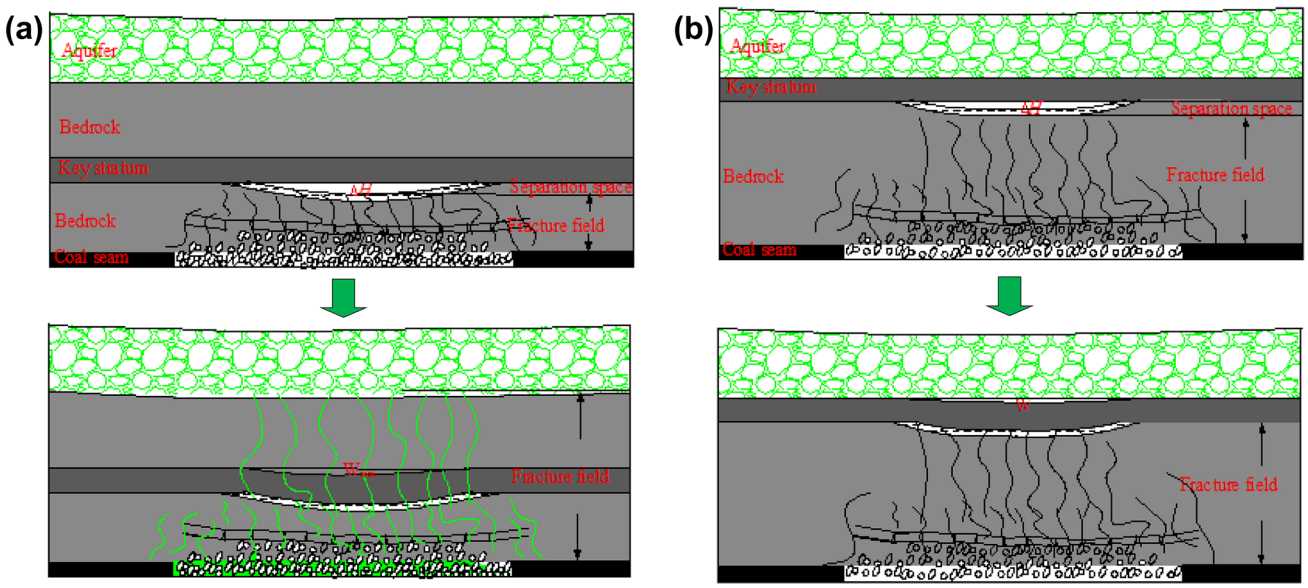

Fig. 9 **a** The mechanism of SFC in lower key stratum situation, **b** the mechanism of SFC in higher key stratum situation

1. The key stratum was distributed as a "ladder shape," associated with heights of 30–75 m in panel #31401. For the lower key stratum, the fracture pattern connected the confined aquifer and triggered the seepage behavior of the stope at heights of 140.5–154.0 m. For the higher key stratum, the fracture field was basically controlled below the key stratum. The time-dependence of the fracturing was identified; the horizontal and vertical fractures occurred sequentially in the confined aquifer, as mining advanced.
2. For the seepage field, the discharge of the LMF increased progressively in the lower key stratum zone, while the rate was negligible for the higher key stratum. The trigger of the water inrush was the increased maximum fracture height in the transition zone between the higher and lower key strata. The abnormal discharge at 120–300 m^3/h along the mining direction commenced in the transition zone, and with the overlying gully serving to replenish the seepage.
3. A fracture height model based on the criteria for the fracture propagation was proposed, interpreting the mechanism between fracture evolution, hydrogeology, and mining technology. A considerable number of highly conductive channels were located near the working face, which were induced by the lower redistributed stress and contributed to the water inrush. Simultaneously, for the areas with a high potential for water inrush, the effect of the SFCC was reduced efficiently by the implementation of a lower mining height, higher mining rate, and enhanced support resistance.

Acknowledgments This paper was supported by the Anhui Provincial Natural Science Foundation (nos. 1908085QE183 and 1808085QE177), Anhui University Scientifc Research Foundation (no. QN2018108), Anhui Province Science and Technology Plan Foundation (nos. 1704a0802129), and the National Key Research and Development Program of China (nos. 2016YFC0801401 and 2016YFC0600708).

References

Booth CJ, Spande ED (1992) Potentiometric and aquifer property changes above subsiding longwall mine panels, Illinois Basin coalfield. Groundwater 30:362–368

Chekan GJ, Listak J (1993) Design practices for multiple-seam longwall mines. US Bureau of Mines Inf Circ 9360, Pittsburgh, PA

Chen X, Su C, Tang X, Guo W (2014) Experimental study of effect of water-saturated state on compaction property of crushed stone from coal seam roof. Chin J Rock Mech Eng 33:3318–3326

Denkhaus BHG (1964) Critical review of strata movement theories and their application to practical problems. Recl des Trav Chim des Pays-Bas 40:519–524

Fawcett RJ, Hibberd S, Singh RN (1986) Analytic calculations of hydraulic conductivities above longwall coal faces. Int J Mine Water 5:45–60. https://doi.org/10.1007/BF02533602

Gu DZ (2015) Theory framework and technological system of coal mine underground reservoir. J Chin Coal Soc 40(2):239–246. https://doi.org/10.13225/j.cnki.jccs.2014.1661

Guo W, Zou Y, Hou Q (2012) Fractured zone height of longwall mining and its effects on the overburden aquifers. Int J Min Sci Technol 22:603–606. https://doi.org/10.1016/j.ijmst.2012.08.001

Karacan CÖ, Goodman G (2009) Hydraulic conductivity changes and influencing factors in longwall overburden determined by slug tests in gob gas ventholes. Int J Rock Mech Min Sci 46:1162–1174. https://doi.org/10.1016/j.ijrmms.2009.02.005

Karacan CÖ, Diamond WP, Esterhuizen GS, Schatzel SJ (2007) Numerical analysis of the impact of longwall panel width on

methane emissions and performance of gob gas ventholes. Int J Coal Geol 71:225–245. https://doi.org/10.1016/j.coal.2006.08.003
Kelly M, Luo X, Craig S (2002) Integrating tools for longwall geomechanics assessment. Int J Rock Mech Min Sci 39:661–676. https://doi.org/10.1016/S1365-1609(02)00063-1
Kratzsch H (1983) Mining subsidence engineering. Springer, Berlin
Lu H, Yuan B, Wang L (2011) Rock parameters inversion for estimating the maximum heights of two failure zones in overburden strata of a coal seam. Min Sci Technol 21:41–47. https://doi.org/10.1016/j.mstc.2010.12.008
Majdi A, Hassani FP, Nasiri MY (2012a) An estimation of the height of fracture zone in Longwall coal mining. J Am Chem Soc 107(14):4343–4345
Majdi A, Hassani FP, Nasiri MY (2012b) Prediction of the height of destressed zone above the mined panel roof in longwall coal mining. Int J Coal Geol 98:62–72. https://doi.org/10.1016/j.coal.2012.04.005
Palchik V (1989) Analytical and empirical prognosis of rock foliation in rock masses. J Coal Ukr 7:45–46
Palchik V (2003) Formation of fractured zones in overburden due to longwall mining. Environ Geol 44:28–38. https://doi.org/10.1007/s00254-002-0732-7
Qian MG (2003) Ground pressure and strata control. The Press of China, University of Mining and Technology, Xuzhou
Rezaei M, Hossaini MF, Majdi A (2015) A time-independent energy model to determine the height of destressed zone above the mined panel in longwall coal mining. Tunn Undergr Sp Technol 47:81–92. https://doi.org/10.1016/j.tust.2015.01.001
Shabanimashcool M, Li CC (2012) Numerical modelling of longwall mining and stability analysis of the gates in a coal mine. Int J Rock Mech Min Sci 51:24–34. https://doi.org/10.1016/j.ijrmms.2012.02.002
Singh MM, Kendorski FS (1981) Strata disturbance prediction for mining beneath surface water and waste impoundments. In: Proceedings of 1st conference on ground control in mining, pp 76–89
Tan X, Konietzky H, Frühwirt T (2014) Laboratory observation and numerical simulation of permeability evolution during progressive failure of brittle rocks. Int J Rock Mech Min Sci 68:167–176. https://doi.org/10.1016/j.ijrmms.2014.02.016
Xie GX, Chang JC, Yang K (2009) Investigations into stress shell characteristics of surrounding rock in fully mechanized top-coal caving face. Int J Rock Mech Min Sci 46:172–181. https://doi.org/10.1016/j.ijrmms.2008.09.006
Xie HP, Mingzhong G, Zhang R, Xu H, Wang YW, Deng JH (2017) The subversive idea and its key technical prospect on underground ecological city and ecosystem. Chin J Rock Mech Eng 36:1301–1313
Xiong DG, Zhao ZM, Su CD, Wang GY (2011) Experimental study of effect of water-saturated state on mechanical properties of rock in coal measure strata. Chin J Rock Mech Eng 30(5):998–1006
Xu JL, Qian MG (2000) Method to distinguish key strata in overburden. J China Univ Min Technol 29(5):463–467
Xu ZM, Sun YJ, Dong QH, Zhang GW, Li S (2010) Predicting the height of water-flow fractured zone during coal mining under the Xiaolangdi reservoir. Min Sci Technol 20:434–438. https://doi.org/10.1016/S1674-5264(09)60222-2
Yang TH, Liu J, Zhu WC, Elsworth D, Tham LG, Tang CA (2007) A coupled flow-stress-damage model for groundwater outbursts from an underlying aquifer into mining excavations. Int J Rock Mech Min Sci 44:87–97. https://doi.org/10.1016/j.ijrmms.2006.04.012
Yuan L (2017) Scientific conception of precision coal mining. J China Coal Soc 42:1
Yuan BX, Chen R, Li JH, Wang YX, Chen WW (2016) A hydraulic gradient similitude testing system for studying the responses of a laterally loaded pile and soil deformation. Environ Earth Sci 75(2):1–7
Yuan BX, Xu K, Wang YX, Chen R, Luo QZ (2017a) Investigation of deflection of a laterally loaded pile and soil deformation using the PIV technique. Int J Geomech 17:04016138. https://doi.org/10.1061/(ASCE)GM.1943-5622.0000842
Yuan L, Zhang T, Zhao YZ, Ren B, Hao XJ, Xu C (2017b) Precise coordinated mining of coal and associated resources A case of environmental coordinated mining of coal and associated rare metal in Odos basin. J Chin Univ MinTechnol 46(3):449–459
Zhang D, Fan G, Ma L, Wang X (2011) Aquifer protection during longwall mining of shallow coal seams: a case study in the Shendong coalfield of China. Int J Coal Geol 86:190–196. https://doi.org/10.1016/j.coal.2011.01.006
Zhao X, Jiang J, Lan B (2015) An integrated method to calculate the spatial distribution of overburden strata failure in longwall mines by coupling GIS and FLAC^{3D}. Int J Min Sci Technol 25:369–373. https://doi.org/10.1016/j.ijmst.2015.03.007
Zheng J, Zheng L, Liu HH, Ju Y (2015) Relationships between permeability, porosity and effective stress for low-permeability sedimentary rock. Int J Rock Mech Min Sci 78:304–318. https://doi.org/10.1016/j.ijrmms.2015.04.025